

Predicting range performance of sampled imagers by treating aliased signal as target-dependent noise

Richard H. Vollmerhausen,^{1,*} Ronald G. Driggers,² and David L. Wilson²

¹760 Jacktown Rd. Lexington, Virginia 24450, USA

²U. S. Army Research, Development, and Engineering Command, Communications and Electronics Research, Development, and Engineering Center, Night Vision and Electronic Sensors Directorate, 10221 Burbeck Rd., Fort Belvoir, Virginia 22060-5806, USA

*Corresponding author: vollmerhausen@hughes.net

Received February 4, 2008; revised June 13, 2008; accepted June 19, 2008;
posted June 20, 2008 (Doc. ID 92409); published July 18, 2008

This paper presents a new theory to predict the impact of sampling on target acquisition. The aliased signal that results from sampling is treated as noise. The aliased signal is different from detector noise in two ways. First, aliasing disappears as the target contrast decreases. Second, the image corruption due to aliasing gets worse with increased range. This is because sampling is constant in angle space, and targets become poorly sampled as range increases. The theory is presented, along with the results of three experiments. The match between model and experiment is excellent. © 2008 Optical Society of America

OCIS codes: 110.3000, 280.4991, 110.3080.

1. INTRODUCTION

Sampling degrades imagery, particularly when the target is at long range. This paper describes a model that predicts the effect of sampling on target acquisition performance. Model theory is described, and model predictions are compared to the results of three tactical-vehicle identification (ID) experiments. The aliasing-as-noise (AAN) theory accurately predicts target probability of identification (PID) at both short and long range.

The impact of sampling on target acquisition performance has been studied for decades; a history of those efforts is found in [1,2]. Two of those efforts have relevance to the current topic. Park and Hazra proposed that aliasing be treated as fixed-pattern noise [3]. However, while they demonstrated that increased variance of the aliased signal results in subjectively degraded imagery, they did not provide a theory or methodology to predict the impact of aliasing on targeting performance.

Driggers, Vollmerhausen, and O’Kane, Mayer, and Krapels proposed the “equivalent blur” (EB) approach to predicting the impact of aliasing on target acquisition [1,2,4,5]. The EB model postulated that the effect of sampling on target recognition and ID depended on the ratio of integrated aliased signal to integrated transfer response; this ratio is called the spurious response ratio (SRR). Further, in-band aliasing below the half-sample frequency affected tasks such as character recognition that require only a few pixels-on-target. In-band aliasing did not affect complex tasks like tactical vehicle ID. Complex tasks required that the target be highly resolved and therefore well-sampled. Aliasing above the half-sample frequency affected all visual tasks. Out-of-band aliasing was associated with visible display-pixel structure; the visible pattern hid the underlying image.

In-band aliasing is caused by inadequate filtering of the scene before sampling. The high-frequency content of the scene is aliased to image frequencies below the half-sample rate of the imager. This corrupts scene information. One assumption of the EB model is that target identification occurs only with the target well resolved. If in-band aliasing exists, it corrupts only small details such as bolts on a tank hatch, and the major structural details remain visible. Therefore, in-band aliasing is ignored by the EB model.

Out-of-band aliasing is image spatial frequency content at frequencies higher than the half-sample rate. Out-of-band aliasing is caused by inadequate postfiltering. For example, large, square display pixels have sharp, visible edges. The frequency content of these visible edges extends beyond the half-sample rate of the imager. This type of aliased signal is at high frequency and does not corrupt information below the half-sample rate. However, this high-frequency, spurious signal tends to mask the underlying image. Out-of-band aliasing disrupts spatial feature generation in the brain and hides the in-band spatial information. The EB model focuses solely on predicting the effect of out-of-band aliasing.

The EB model distinguishes imagery into two imaging categories: well-sampled and poorly sampled. Visible display-pixel structure hurts even well-sampled images. In-band aliasing degrades poorly sampled images. The EB model provides a “rule-of-thumb” correction to degrade performance due to display artifacts. However, the EB model does not handle the transition from well-sampled to poorly sampled as range increases.

Minimum temperature difference perceived (MTDP) and triangle orientation discrimination (TOD) are two recent models for predicting performance of sampled imag-

ers [6,7]. These models are intimately associated with the concept that an imager's limiting resolution predicts PID. MTDP and TOD cannot be used with image quality metrics that depend on the entirety of the imager's frequency response. Specifically, MTDP and TOD cannot be used with the targeting task performance (TTP) metric. TTP is a much better predictor of the effect of imager blur and noise on PID than limiting resolution metrics such as the Johnson criteria [8].

The tactical-vehicle ID experiments described in this paper were originally performed to validate the EB model. However, in these experiments, in-band aliasing affected tactical-vehicle ID. Also, sampling had a greater effect at long range than at short range. The EB model failed to predict either experimental result described below.

The original EB experiment was reviewed to explain the apparent contradiction in results. For the in-band aliasing experiment described in [2], the tactical vehicle range was constant at 670 meters, and the imager field-of-view (FOV) was 3.2° . Changing imager F-number, detector size, and detector pitch generated aliasing that distorted target details. However, there were 200 pixels on target even at the widest sample spacing. Identification cues such as the number of road-wheels, engine location, and bulk silhouette of the vehicle were still recognizable to the trained observers. The conclusion of [2] that in-band aliasing had a measurable but small effect on target ID was correct for that experiment.

The effect of imager sampling on target ID is range dependent. For a particular imager, the angle in milliradians between samples is fixed, but the sample spacing *in meters on the target* increases as range increases. The target becomes poorly sampled at longer ranges. Figure 1 illustrates the effect of increased sample spacing. In that figure, the focal plane array (FPA) has a 0.18 fill-factor both horizontally and vertically. The numerals become more difficult to read as range increases in five foot increments from 10 feet to 25 feet. The linear spacing between samples increases with range, and the corruption due to aliasing is range dependent.

This paper compares the predictions of both the AAN and EB models to the results of tactical-vehicle ID experiments where range is varied. In these experiments, PID represents the fraction of a group of similar-scale but diverse-looking objects that are correctly identified. The tactical-vehicle target set consists of tanks, armored personnel carriers, and self-propelled howitzers. Some of the vehicles look alike and are correctly identified only at short range. Other vehicles in the set are distinctive and

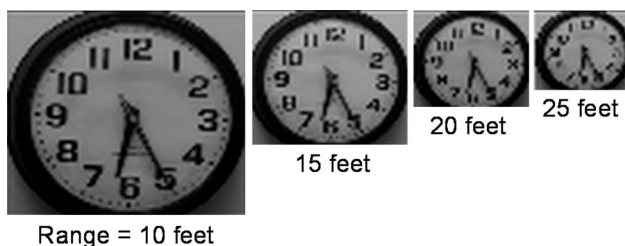


Fig. 1. Pictures of a clock taken with an undersampled imager. The numerals become harder to read as range increases.

are identified at longer range. Models that predict the fraction of objects correctly identified at each range are commonly called detect, recognize, and identify (DRI) models.

The DRI model applies to groups of objects that share a similar scale. For example, the model applies to a group of hand-held objects or a group of tactical vehicles. It is assumed that the objects in each group are sufficiently diverse that all spatial frequencies are equally important to discriminate between objects in the group. Considering all the targets and target aspects to be identified at each range, the assumption underlying the DRI model is that discrimination cues exist equally at all spatial frequencies.

Probabilities are predicted using the TTP metric [8,9]. TTP predicts the effect of imager blur and noise on observer visual-task performance. That is, TTP correlates with PID, so that PID is a function of the TTP value. The EB model accounts for sampling by degrading TTP resolution by a fixed amount based on the SRR. To implement the AAN model, aliasing is treated as noise. Aliasing degrades TTP resolution in the same way that detector noise degrades resolution. Aliasing is treated as fixed-pattern noise that changes with range.

It is expected that the AAN model also predicts the results of the character recognition experiment described in [1]. However, predicting the probability of character recognition requires the use of a specific object model (SOM). Vollmerhausen and Robinson discuss the differences between the SOM and DRI models and the correct application of each model [9]. The SOM predicts the probability of identifying a particular object. To do this, the Fourier transform of the object is incorporated into the model. The experiment in [1] used equally recognizable block characters. Discrimination cues reside in a limited band of spatial frequencies, and the DRI assumption that all spatial frequencies are equally important does not apply. The SOM is structurally different from the DRI model, and only the DRI model is addressed.

The calculation of aliased signal is described in Section 2. Section 3 describes the TTP metric and explains how aliasing is incorporated into the model. Section 4 summarizes three tactical-vehicle identification experiments. In Section 5, experimental results are compared with model predictions. Conclusions are in Section 6. Appendix A is a glossary of acronyms and symbols used in the paper.

2. CALCULATION OF ALIASED SIGNAL

A detailed derivation of the Fourier transform $O(\xi, \eta)$ of a sampled image is provided by [1]. Equation (1) repeats Eq. (6) of [1]:

$$O(\xi, \eta) = [I(\xi, \eta)H_{\text{pre}}(\xi, \eta) ** \text{comb}(a\xi, b\eta)]D(\xi, \eta). \quad (1)$$

$$O(\xi, \eta) = \left[I(\xi, \eta)H_{\text{pre}}(\xi, \eta) ** \sum_{m=0}^{\infty} \sum_{n=0}^{\infty} \delta \right. \\ \left. \times (\xi - n/a, \eta - m/b) \right] D(\xi, \eta), \quad (2)$$

where $**$ denotes two-dimensional convolution. Equation

(2) follows from the definition of the comb function. Definitions follow for these and following equations:

ξ ≡ horizontal spatial frequency in cycles per milliradian (mrad)

η ≡ vertical spatial frequency in cycles per mrad

a ≡ horizontal detector pitch in mrad

$\nu \equiv 1/a$; ν is the horizontal sample frequency in milliradians⁻¹

b ≡ vertical detector pitch in milliradians

$\gamma \equiv 1/b$; γ is the vertical sample frequency in milliradians⁻¹

$I(\xi, \eta)$ ≡ Fourier transform of object radiance distribution

H_{pre} ≡ presample modulation transfer function (MTF) including optical diffraction, optical aberrations, and detector spatial integration

$D(\xi, \eta)$ ≡ postsample MTF including digital processing and display MTF.

The term with both m and n equal to zero is the uncorrupted signal term or transfer response. The Fourier transform of the aliased signal $A(\xi, \eta)$ constitutes the remaining terms.

$$A(\xi, \eta) = \left[I(\xi, \eta) H_{\text{pre}}(\xi, \eta) * * \sum_{m \neq 0}^{\infty} \sum_{n \neq 0}^{\infty} \delta \right. \\ \left. \times (\xi - n/a, \eta - m/b) \right] D(\xi, \eta). \quad (3)$$

In the DRI model, $I(\xi, \eta)$ is assumed to be white (that is, spectrally uniform). If target radiance contrast is T_{con} in watts per square meter per steradian ($\text{w m}^{-2} \text{sr}^{-1}$), then

$$A(\xi, \eta) = \left[T_{\text{con}} H_{\text{pre}}(\xi, \eta) * * \sum_{m \neq 0}^{\infty} \sum_{n \neq 0}^{\infty} \delta \right. \\ \left. \times (\xi - n/a, \eta - m/b) \right] D(\xi, \eta) \quad (4)$$

$$= \left[T_{\text{con}} \sum_{m \neq 0}^{\infty} \sum_{n \neq 0}^{\infty} H_{\text{pre}}(\xi - n\nu, \eta - m\gamma) \right] D(\xi, \eta). \quad (5)$$

Note that Eq. (5) is correct for surfaces characterized by functions of ξ and η ; these surfaces have a radiance distribution that is constant in imager angle-space regardless of range.

3. DESCRIPTION OF DRI TARGET ACQUISITION MODEL

The ability of an observer to resolve a target at range R_{ng} is quantified by the TTP metric (Φ). Model implementation and validation for nonsampled imagery is described in detail in [8,10]. In the DRI model, functions are assumed separable in Cartesian coordinates, and Φ is the geometric mean of horizontal and vertical resolution. Φ quantifies resolution of a surface at range R_{ng} and has units of cycles per meter:

$$\Phi = \left[\int \sqrt{\delta \left(\frac{C_{\text{TGT}}}{\text{CTF}_{\text{sys}}(\xi)} \right) \frac{C_{\text{TGT}}}{\text{CTF}_{\text{sys}}(\xi)} \frac{d\xi}{R_{\text{ng}}} } \right. \\ \left. \times \int \sqrt{\delta \left(\frac{C_{\text{TGT}}}{\text{CTF}_{\text{sys}}(\eta)} \right) \frac{C_{\text{TGT}}}{\text{CTF}_{\text{sys}}(\eta)} \frac{d\eta}{R_{\text{ng}}} } \right]^{1/2}. \quad (6)$$

All of the sampling experiments considered here use equal horizontal and vertical resolution. To simplify the discussion, only the equations for horizontal resolution are described.

$$\Phi = \int \sqrt{\delta \left(\frac{C_{\text{TGT}}}{\text{CTF}_{\text{sys}}(\xi)} \right) \frac{C_{\text{TGT}}}{\text{CTF}_{\text{sys}}(\xi)} \frac{d\xi}{R_{\text{ng}}} }, \quad (7)$$

where C_{TGT} is target modulation contrast given by

$$C_{\text{TGT}} = \frac{T_{\text{con}}}{2SCN}. \quad (8)$$

SCN is the scene radiance in $\text{w m}^{-2} \text{sr}^{-1}$ that generates the average display luminance. SCN sets the gain of the imager; it is the difference in scene radiance that raises display luminance from black to average.

CTF_{sys} is naked-eye contrast threshold function (CTF) degraded by imager blur and noise. The analyses in this paper use a numerical approximation to measured naked-eye CTF published by Barten [11]. Equation (9) fits data from two-alternative-forced-choice experiments. The observer is shown two display locations, one with a sine wave pattern and one without. The observer must pick the location containing the sine wave pattern. CTF is the sine wave contrast resulting in correct observer choice half the time independent of chance. Data are collected for many bar-pattern sizes and for different display luminances.

$$\text{CTF}(\xi) = [a\xi e^{-b\xi} \sqrt{1 + 0.06e^{b\xi}}]^{-1}, \quad (9)$$

where

$$a = \frac{540 \left(1 + \frac{0.2}{L} \right)^{-0.2}}{12} \quad \text{and} \quad b = 5.24 \left(1 + \frac{29.2}{L} \right)^{0.15} \\ 1 + \frac{w_a^2}{1 + 5.8\xi^2} \quad (10)$$

The independent variables are the luminance of the display (L) in foot-Lamberts (fL) and the square root of the angular object or display size (w_a) in degrees.

The effect of blur and detector noise on naked-eye CTF is described in [8,10,12,13]. Equation (11) gives CTF degraded by imager blur and noise:

$$\text{CTF}_{\text{sys}}(\xi) = \frac{\text{CTF} \left(\frac{\xi}{\text{smag}} \right)}{H_{\text{sys}}(\xi)} \left(1 + \frac{\alpha^2 \Gamma_{\text{det}}^2 Q(\xi, \eta)}{SCN^2} \right)^{1/2}, \quad (11)$$

where smag is the system magnification (the angle subtended at the eye by the target image divided by the angle subtended by the target at the imager). Other factors include

$\alpha \equiv 169.6$ (a proportionality constant with unit root-Hertz)

$B(\xi)$ =noise filters in visual cortex [8,11]

$H_{\text{eye}}(\xi)$ =eyeball MTF [8,14]

$H_{\text{sys}}(\xi)$ =system MTF from scene to display

$Q(\xi, \eta)$ =noise bandwidth defined by Eq. (12) below

Γ_{det} ≡noise standard deviation with units $\text{s}^{1/2} \text{ w m}^{-2} \text{ sr}^{-1} \text{ mrad}$

$$Q(\xi, \eta) = \int_{-\infty}^{\infty} \left| B\left(\frac{\xi}{\text{smag}}\right) D(\xi) H_{\text{eye}}\left(\frac{\xi}{\text{smag}}\right) \right|^2 \times d\xi \int_{-\infty}^{\infty} \left| D(\eta) H_{\text{eye}}\left(\frac{\eta}{\text{smag}}\right) \right|^2 d\eta. \quad (12)$$

δ is the probability of seeing a sine wave with amplitude C_{TGT} , given that the 0.5 threshold of the eye is CTF_{sys} . Assuming that the signal is visible above threshold and invisible below threshold results in little error when calculating Φ :

$$\delta\left(\frac{C_{\text{TGT}}}{\text{CTF}_{\text{sys}}(\xi)}\right) \begin{cases} =1 & \text{for } \frac{C_{\text{TGT}}}{\text{CTF}_{\text{sys}}(\xi)} \geq 1 \\ =0 & \text{for } \frac{C_{\text{TGT}}}{\text{CTF}_{\text{sys}}(\xi)} < 1 \end{cases}. \quad (13)$$

There is a single calibration constant α in the DRI model, which is a proportionality constant that quantifies the effect of noise on human CTF. α is found empirically with CTF experiments and other experiments examining the effect of noise on threshold [8,10].

The difficulty of identifying a target depends on how much the target looks like other objects in the target set. Φ_{84} is the value of Φ that results in 0.84 probability of task performance; it is determined empirically for each target set. For the experiments described here, Φ_{84} is 15.6 based on the blur and noise experiments reported in [8]. The PID is a function of the ratio Φ to Φ_{84} [15]:

$$\text{PID}(\Phi/\Phi_{84}) = \text{erf}(\Phi/\Phi_{84}) = \frac{2}{\sqrt{\pi}} \int_0^{\Phi/\Phi_{84}} e^{-t^2} dt. \quad (14)$$

To predict PID versus range, the following procedure is used: The naked-eye CTF is degraded by imager blur and noise to establish CTF_{sys} . Φ is found at each range by a numerical integration corresponding to Eq. (7). PID is predicted using Φ in Eq. (14).

A. Incorporating Aliasing into the Target Acquisition Model

Aliasing acts like noise because of the DRI task. At all ranges, observers attempt to identify each member of a target set. The size and placement of identification cues varies from target to target. At short range, aliasing obscures few or none of the target cues. As range increases, more and more target cues are corrupted by aliasing. Aliasing acts like noise because of the combination of multiple target identifications, diversity in the size and placement of visual cues, and the random sample-phase of each target detail.

To model the effect of aliasing on PID, calculate the square root of the sum of the squares (RSS) of the aliased signal and the detector noise. Both detector noise and

aliased signal are expressed as modulation on the average display luminance by dividing by 2 SCN . The factor of two is incorporated into the calibration constant α . Aliasing increases noise and therefore degrades (elevates) CTF_{sys} . Using the degraded CTF_{sys} in Eq. (7) results in poorer resolution of the target and reduced PID.

In order to determine the RSS of the aliased signal in Eq. (5) with detector noise, it must be properly scaled. Detector noise varies randomly in both space and time. The eye integrates signal and noise for a time period that is light-level dependent. Since the noise is random, the signal-to-noise ratio improves as the $\sqrt{t_{\text{eye}}}$. However, the model calibration constant α is based on averaging noise over a full second. The model degrades signal to noise by the $\sqrt{1/t_{\text{eye}}}$. Aliasing is fixed-pattern noise; the signal-to-noise ratio is not time dependent. The aliased signal is multiplied by the $\sqrt{t_{\text{eye}}}$ to remove the model correction.

Also, Eq. (5) is two-dimensional, whereas we are calculating only horizontal CTF_{sys} . Equation (15) below represents the aliasing that masks the horizontal signal. δ is the Dirac delta function. Note that, like all images, a CTF bar pattern is two-dimensional. The equation represents horizontal aliasing and uniform intensity vertically:

$$A(\xi, \eta) = \left[\sqrt{t_{\text{eye}}} T_{\text{con}} \sum_{m \& n \neq 0} H_{\text{pre}}(\xi - n\nu) \delta(\eta - 0) \right] D(\xi) D(\eta). \quad (15)$$

In the model, detector noise and signal are integrated over a milliradian both horizontally and vertically. The calibration constant α is based on averaging signal-to-noise ratio over a square milliradian. Γ_{det} has units of $\text{s}^{1/2} \text{ w m}^{-2} \text{ sr}^{-1} \text{ mrad}$, and the detector noise term in Eq. (11) (the second term in the brackets) is unitless.

CTF_{sys} for the AAN model is given by Eqs. (16) and (17) below. At each spatial frequency, the aliased signal, filtered by the eye and visual cortex, is squared and then integrated. Equation (16) involves an infinite sum. However, the display and the eye filter high spatial frequencies. Only a few of the terms are numerically significant:

$$\text{CTF}_{\text{sys}}(\xi) = \frac{\text{CTF}\left(\frac{\xi}{\text{smag}}\right)}{H_{\text{sys}}(\xi)} \left(1 + \frac{\alpha^2 \Gamma_{\text{det}}^2 Q(\xi, \eta)}{\text{SCN}^2} + \frac{\alpha^2 t_{\text{eye}} T_{\text{con}}^2 R_{\text{ng}}^2 Q_a(\xi, \eta)}{\text{SCN}^2} \right)^{1/2}, \quad (16)$$

where

$$Q_a(\xi, \eta) = \int_{-\infty}^{\infty} \delta(\eta - 0) D(\eta) d\eta \int_{-\infty}^{\infty} \left| \sum_{\substack{n=-\infty \\ n \neq 0}}^{\infty} H_{\text{pre}}(\xi - n\nu) \right|^2 \times B\left(\frac{\xi}{\text{smag}}\right) D(\xi) H_{\text{eye}}\left(\frac{\xi}{\text{smag}}\right) d\xi. \quad (17)$$

Note that the proportionality constant α is the same for all noise terms. The AAN model does not require a separate calibration constant. The R_{ng}^2 factor properly scales

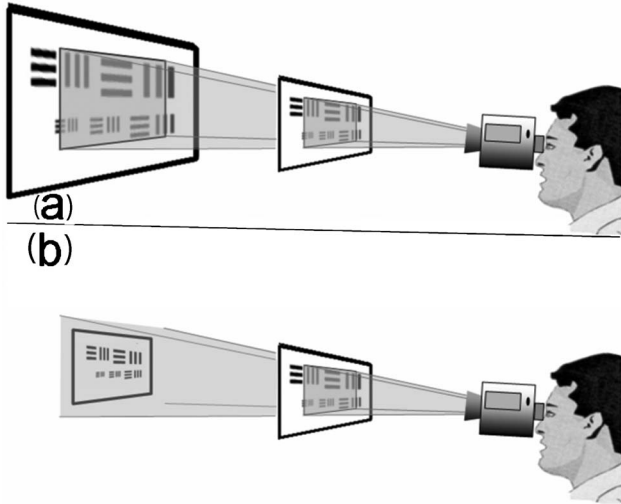


Fig. 2. Linear size of bar chart at top (a) grows in proportion to range. The linear size of bar chart at bottom (b) is constant.

amplitude and results in the correct units. This is discussed in the next subsection.

B. Discussion of Range-Squared Scaling of the Aliased Signal

Two aspects of the R_{ng}^2 factor in Eq. (16) are discussed in this subsection. First, the physical reasoning behind the factor is explained. Next, units are discussed.

In the DRI model, target radiance $I(\xi, \eta)$ and detector noise are functions of ξ and η . This is convenient, because the impact of detector noise on performance is constant in angle space. The model predicts imager resolution in cycles per milliradian. However, imager resolution is converted to cycles per meter on target when predicting PID at a specific range. The relationship between cycles per meter (ξ_m) and cycles per milliradian is given by Eq. (18):

$$\xi_m = \frac{\xi}{R_{ng}}. \quad (18)$$

At the top of Fig. 2, the bar chart is represented by $I(\xi, \eta)$; the chart gets linearly larger in proportion to range from the imager. A physical target behaves as

shown at the bottom of Fig. 2. The bottom bar chart is represented by $I_m(\xi_m, \eta_m)$, where ξ_m and η_m are spatial frequencies in cycles per meter on the target. The bottom chart has a fixed, linear size and gets smaller in angle relative to the imager as range increases. In the imager's frequency domain, target spectrum spreads as range increases. At any one range, the functions $I(\xi, \eta)$ and $I_m(\xi_m, \eta_m)$ are related in a known way, but the relationship is range dependent.

Let $I_m(\xi_m, \eta_m)$ represent a target with constant linear dimension and spectrally uniform Fourier transform. $G(\xi, \eta, R_{ng})$ is the angular radiance distribution at the imager. $G(\xi, \eta, R_{ng})$ and $I_m(\xi_m, \eta_m)$ are related by Eq. (19) below. For a real target of fixed, linear size, the target signal within the imager bandwidth decreases with range:

$$G(\xi, \eta, R_{ng}) = \frac{I_m(\xi/R_{ng}, \eta/R_{ng})}{R_{ng}^2}. \quad (19)$$

As the angular size of the target becomes smaller with increased range, the frequency spectrum in the imager decreases in amplitude and broadens in frequency. The physical reality is that the ratio of signal to aliased noise decreases in proportion to range squared because the signal is falling, not because aliasing within the imager is growing. However, the model assumes that target structure grows with range. Given the constant, range-independent signal assumed by the model, the aliased signal in Eq. (16) must grow as range squared.

The aliasing term in Eq. (16) is unitless. To show this, consider a surface that is constant in angle-space as shown at the top of Fig. 2. For a surface with radiance of the form $I(\xi, \eta)$, T_{con} generates a signal spectral density (SSD) of $T_{con} \text{ w m}^{-2} \text{ sr}^{-1} \text{ mrad}$ in the frequency domain of imager angle-space. This is consistent with the use of T_{con} as a SSD in Eqs. (7) and (8). SCN is the surface radiance necessary to generate the average display luminance. For the aliasing term, however, the surface is a fixed, linear size. A surface of fixed, linear size with radiance $SCN \text{ w m}^{-2} \text{ sr}^{-1}$ creates a SSD of $SCN \text{ w m}^{-2} \text{ sr}^{-1} \text{ m}$. Dividing by R_{ng} converts from meter to milliradian. As shown by Eq. (20), the units for the aliasing term are milliradian⁻²:

$$\text{aliasing noise (units)} \equiv \frac{\alpha^2(\text{Hertz})t_{eye}(\text{second})T_{con}^2(\text{w m}^{-2} \text{ sr}^{-1} \text{ mrad})^2R_{ng}^2(\text{m}^2 \text{ mrad}^{-2})ff(\text{mrad})^{-2}}{SCN^2(\text{w m}^{-2} \text{ sr}^{-1} \text{ m})^2}. \quad (20)$$

The aliasing term in Eq. (16) (the third term in the brackets) is unitless except for a milliradian² in the denominator. A milliradian is unitless, but it is best to remove this ambiguity.

Rather than viewing SCN as the radiance that generates the average display luminance, SCN can be viewed as the SSD that generates the average display luminance.

The calibration constant α is applied to signal-to-noise ratio terms that are averaged over a milliradian. Make the application of α explicit by applying the units $\sqrt{\text{Hertz mrad}}$.

The units of the detector and aliasing terms in Eqs. (11) and (16) are now given by Eqs. (21) and (22), respectively, below. Both noise terms are unitless:

$$\text{detector noise (units)} \equiv \frac{\alpha^2(\text{Hertz mrad}^2)\Gamma_{\text{det}}^2(\text{second}^{1/2} \text{ w m}^{-2} \text{ sr}^{-1} \text{ mrad})^2 \text{ff}(\text{mrad})^{-2}}{\text{SCN}^2(\text{w m}^{-2} \text{ sr}^{-1} \text{ mrad})^2}, \quad (21)$$

$$\text{aliasing noise (units)} \equiv \frac{\alpha^2(\text{Hertz mrad}^2)t_{\text{eye}}(\text{second})T_{\text{con}}^2(\text{w m}^{-2} \text{ sr}^{-1} \text{ mrad})^2 R_{\text{ng}}^2(\text{m}^2 \text{ mrad}^{-2}) \text{ff}(\text{mrad})^{-2}}{\text{SCN}^2(\text{w m}^{-2} \text{ sr}^{-1} \text{ m})^2}. \quad (22)$$

As range increases, the signal from each point on the target decreases, but the target area covered by an imager sample increases proportionally. Therefore, an aliased signal is constant with range. However, the target radiance is fixed in linear space; it is not fixed in imager angle-space. As range increases, the target frequency spectrum spreads in the imager frequency domain. Spreading of the target spectrum makes the impact of aliasing range dependent.

4. TACTICAL VEHICLE ID EXPERIMENTS

This section describes three tactical-vehicle ID experiments. Further details on these experiments are found in [5,8]. The twelve-vehicle target set includes tanks, armored personnel carriers, and self-propelled howitzers. Twelve aspects of each vehicle result in 144 images. Pristine thermal images are collected at short range. The images are processed using MATLAB to simulate various imagers with the targets at selected ranges. The use of simulation ensures the accuracy of blur and other imager characteristics. All observers are trained, active military in specialties such as tank gunner, aircraft gunner, or photo interpreter.

Although 144 images is a large picture set, subjects quickly learn to associate a particular shading or hot spot location or background with the particular target. When that happens, the target is known, and feature discrimination is no longer necessary. To prevent learning during the test, each picture is used at most six times in each experiment. A different set of 24 vehicle aspects is used at each of six ranges. The target subsets are balanced in terms of task difficulty by ensuring that all aspects and all vehicles are equally represented in each subset. How-

ever, variation in task difficulty between subsets is one significant source of experimental error.

Experiment 25 represents a thermal imager with realistic amounts of in-band aliasing. Different display interpolations are used to explore the effect of visible pixel structure on performance. Replicated pixels cause visible edges that interrupt the eye's ability to integrate the underlying scene. Bicubic and, to a lesser extent, bilinear interpolation smooths the pixel edges and improves performance.

Experiment 25 used a midwave infrared (IR), staring focal plane array with 256 by 256 detectors. The active detector area was 28 μm on a 30 μm pitch. The sensor field of view was 2° by 2°. The F/2 optics had a 22 cm focal length. The simulated ranges were 0.54 to 3.24 km in 0.54 km increments. The imagery was displayed on a high-resolution, monochrome monitor.

Experiment 25 consisted of six lines each with six ranges. Each line used different interpolations to increase image size. The use of different display interpolations changed the character of the displayed image by adding different types of pixel structure. The display interpolation for each line is shown in Table 1. Each cell consisted of 24 images processed with the same display interpolation and E-zoom and with the target at the same range.

Figure 3 shows the alias and transfer frequency spectra in one dimension; the imager has symmetrical resolution in the horizontal and vertical. The abscissa is spatial frequency in cycles per mrad. The ordinate is amplitude. The transfer response changed little between lines. Aliasing is shown for lines 1 and 4; these lines represent the maximum aliasing for each display zoom. The half-sample frequency was 3.7 mrad^{-1} . Aliasing is present both above and below the half-sample frequency. This amount of

Table 1. Display Interpolations^a, System Magnifications, and Detector Fill-Factors for Sampling Experiments

| Experiment No. & Line | First Intrp | Second Intrp | Third Intrp | Sys Mag | Fill-Fac |
|-----------------------|-------------|--------------|-------------|---------|----------|
| 25 line 1 | none | Replicate | Replicate | 9 | Large |
| 25 line 2 | none | Bilinear | Replicate | 9 | Large |
| 25 line 3 | none | Bicubic | Replicate | 9 | Large |
| 25 line 4 | Replicate | Replicate | Replicate | 18 | Large |
| 25 line 5 | Bilinear | Bilinear | Replicate | 18 | Large |
| 25 line 6 | Bicubic | Bicubic | Replicate | 18 | Large |
| 36 line 1 | none | none | Bicubic | 10.6 | Large |
| 36 line 2 | none | none | Replicate | 10.6 | Large |
| 36 line 3 | none | none | Bicubic | 10.6 | Small |
| 36 line 4 | none | none | Replicate | 10.6 | Small |

^aIntrp stands for interpolations, sys mag for system magnifications, and fill-fac for fill-factors.

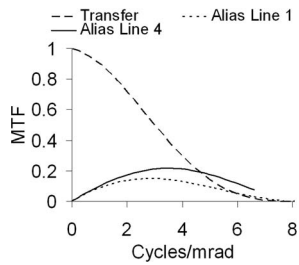


Fig. 3. Alias spectrum and transfer response for experiment 25, lines 1 and 4.

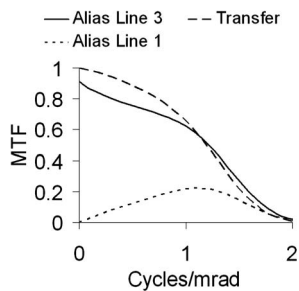


Fig. 4. Alias spectrum and transfer response for experiment 36, lines 1 and 3.

aliasing is not unusual for an imager with a 256 by 256 detector array.

Experiment 36 was performed to explore the impact of large amounts of aliasing on targeting performance. Again, a 256 by 256 focal plane array was used. The F/2 optics had a 7.33 cm focal length. Imagery was displayed on a high-resolution, monochrome monitor. Simulated ranges are 0.43, 0.64, 0.97, 1.3, 1.6, and 2.15 km. Changing detector active area (detector fill-factor) and display interpolation creates various amounts and types of aliasing. Low aliasing results from setting the detector size to 25 by 25 μm (100% fill-factor). High aliasing results from setting the detector size to 1 by 1 μm (fill-factor of 1/25 in both directions). This small fill-factor greatly increases aliasing. With F/2 optics, the blur due to spatial integration of the scene over the detector area is a significant presample filter. Reducing the detector area to 1 by 1 μm removes this significant presample blur and results in substantially increased aliasing. To change display pixel visibility, different display interpolations were used; these are listed in Table 1.

Figure 4 shows experiment 36 alias frequency spectrum and transfer response. The abscissa is spatial frequency in cycles per milliradian and the ordinate is amplitude. Only lines 1 and 3 are shown because these are representative of lines 2 and 4; the effect of interpolation was small compared to the effect of fill-factor. The half-sample frequency is 1.5 mrad^{-1} . Line 1 has a large fill-factor, and the aliasing is similar to the aliasing in experiment 25. Line 3 has a small fill-factor and therefore substantial aliasing.

Experiment 21 was designed to determine the effect of shifting the aliased signal on the frequency axis. It consisted of four experiments labeled (a) through (d). Experiment 21(a) had zero aliasing, and Experiment 21(d) had maximum aliasing. Each experiment consisted of three lines with approximately the same integrated amount of aliased signal. The aliased signal was centered below, at, or above the half-sample frequency and therefore represented in-band, mid-band, or out-of-band aliasing, respectively. So experiment 21(a) through (d) had increasing amounts of aliasing, and in each experiment, lines 1 through 3 represent in-band, mid-band, and out-of-band aliasing, respectively.

The six cells in each line used a different presample blur, downsample, and postsample blur. The presample and postsample blurs took the form

$$c_i = \text{sinc}\left(\frac{i}{b}\right) \exp\left[-\pi\left(\frac{i}{4b}\right)^2\right], \quad (23)$$

where c_i was the i th coefficient of an odd digital filter.

Table 2 gives the presample blur size, downsample value, and postsample blur size for each cell. For example, the notation 5/2/8 represents a pre blur size of $b=5$, a downsample of $b=2$, and a postblur size of $b=8$. Figure 5 shows the transfer response and aliased signal for cell F of experiment 21(d), lines 1, 2, and 3. The half-sample frequency is 0.14 mrad^{-1} . These cells represent the most aliasing used in experiment 21. The figure shows the in-band (line 1), mid-band (line 2), and out-of-band (line 3) position of the aliased signal.

Ten observers took experiment 21, 20 observers took experiment 25, and 23 observers took experiment 36. All images in a cell were presented sequentially but the cells were randomized. Results were corrected for chance and mistakes [8].

Table 2. Preblur, Downsample, Postblur for Each Cell of Experiment 21

| Experiment&Line | Cell A | Cell B | Cell C | Cell D | Cell E | Cell F |
|-----------------|-----------|-----------|-----------|----------|----------|----------|
| 21(a) Line 1 | 0/1/5 | 0/1/10 | 0/1/15 | 0/1/20 | 0/1/25 | 0/1/30 |
| 21(a) Line 2 | 5/1/5 | 10/1/10 | 15/1/15 | 20/1/20 | 25/1/25 | 30/1/30 |
| 21(a) Line 3 | 5/1/0 | 10/1/0 | 15/1/0 | 20/1/0 | 25/1/0 | 30/1/0 |
| 21(b) Line 1 | 3.2/4/5 | 6.4/8/10 | 9.6/12/15 | 13/16/20 | 16/20/25 | 20/25/30 |
| 21(b) Line 2 | 3.8/4/3.8 | 7.6/8/7.6 | 11/12/11 | 15/16/15 | 19/20/19 | 24/25/24 |
| 21(b) Line 3 | 5/4/3.2 | 10/8/6.5 | 15/12/9.5 | 20/16/13 | 25/20/16 | 30/25/20 |
| 21(c) Line 1 | 2.9/4/5 | 5.8/8/10 | 8.9/12/15 | 12/16/20 | 15/20/25 | 19/25/30 |
| 21(c) Line 2 | 3.6/4/3.6 | 7.1/8/7.1 | 11/12/11 | 14/16/14 | 18/20/18 | 22/25/22 |
| 21(c) Line 3 | 5/4/2.9 | 10/8/5.9 | 15/12/8.7 | 20/16/12 | 25/20/15 | 30/25/19 |
| 21(d) Line 1 | 2.7/4/5 | 5.4/8/10 | 8.2/12/15 | 11/16/20 | 14/20/25 | 17/25/30 |
| 21(d) Line 2 | 3.4/4/3.4 | 6.7/8/6.7 | 10/12/10 | 13/16/13 | 17/20/17 | 21/25/21 |
| 21(d) Line 3 | 5/4/2.8 | 10/8/5.5 | 15/12/8.2 | 20/16/11 | 25/20/14 | 30/25/17 |

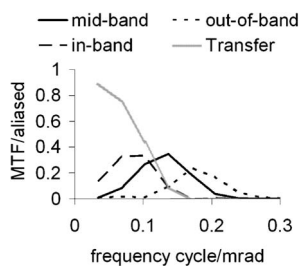


Fig. 5. Alias spectra and transfer response for Experiment 21(d), cell F. In-band aliasing is line 1, mid-band is line 2, and out-of-band is line 3.

5. EXPERIMENTAL RESULTS AND MODEL PREDICTIONS

In this section, the predictions of the AAN and EB models are compared with data from experiments 21, 25, and 36. Figures 6–9 compare model and data for experiment 36. Figures 10–15 show results for experiment 25. In each figure, the abscissa is range in km and the ordinate is PID. The dashed curves show model predictions with no correction for aliasing (NC). The solid curves show predictions corrected using the EB model (EB). The dotted curves show predictions corrected using the AAN model (AAN). Data are shown with open diamonds.

Figure 16 shows model to data comparisons for experiment 21: The abscissa is measured PID, and the ordinate is model PID. Open circles indicate AAN predictions, plus signs, for the EB model, and small filled circles, no sampling correction. Model predictions that lie on the solid line are a perfect match with data.

Table 3 gives the root-mean-square-error (RMSE) and coefficient of determination (COD) for all experiments and all three models. Note that no new parameters are used to fit AAN predictions to data. The constant factor α is the same gain factor used for detector noise; AAN acts like noise and does not need a separate calibration factor. Also note that the EB model is calibrated using the results of experiment 21; a good fit between EB predictions and experiment 21 data is therefore expected. For all experiments, the fit between AAN model predictions and data is excellent.

Looking at Figs. 13–15, the AAN model is somewhat pessimistic for experiment 25, lines 4 through 6. These lines use a system magnification of 18, making the sampling artifacts quite visible. Normally, observers would move their heads back, away from the display, making the image easier to interpret. Eye MTF is an effective filter of out-of-band aliasing. However, in this experiment, observers were placed in a steeply-reclined chair with a fixed viewing distance. The discrepancy between model and data is not explained by head motion. The actual cause of the pessimistic predictions is not understood, but the model errors are not large.

In experiment 36, observers were seated in chairs without rollers and with a fixed but gentle recline. Observers were asked to maintain a nominal display-to-eye distance of ≈ 46 cm but could move their heads backward to ≈ 60 cm. Using a 60 cm viewing distance results in a small improvement in model accuracy; COD is 0.92 and RMSE is 0.077. For this experiment, display-to-eye distance had a negligible effect on model predictions.

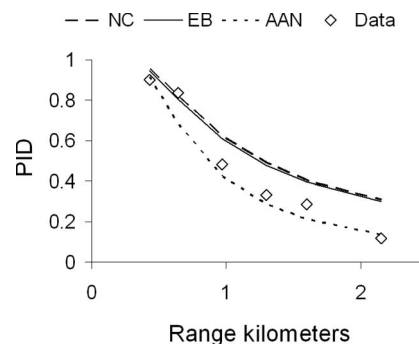


Fig. 6. PID versus range for experiment 36, line 1.

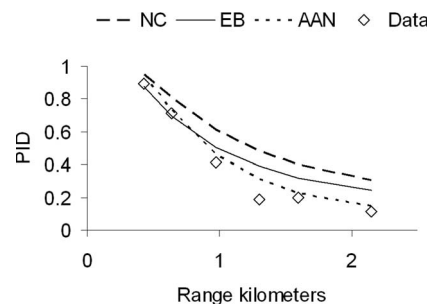


Fig. 7. PID versus range for experiment 36, line 2.

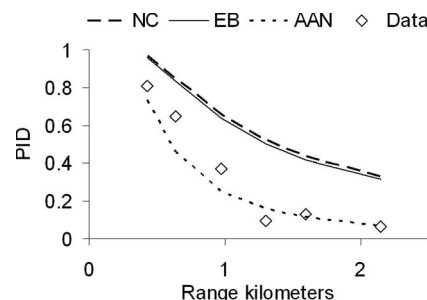


Fig. 8. PID versus range for experiment 36, line 3.

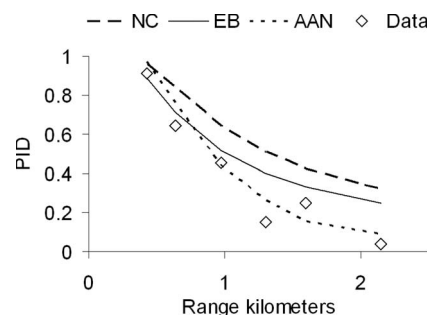


Fig. 9. PID versus range for experiment 36, line 4.

During Experiment 21, the observers were not warned to limit head motion, and they were observed constantly moving their heads. Further, the aliased signal was always near the half-sample frequency. Head motion provided an effective anti-aliasing filter that could be tuned to a particular image. Figure 17 shows model predictions when head motion is allowed to vary between 30 and 75 cm. COD for NC, EB, and AAN are 0.98, 0.99, and 0.98, respectively. Head motion explains most of the prediction errors observed in Fig. 16.

The AAN model provides a much better fit to data than the EB model. COD and RMSE both indicate a good fit between AAN predictions and experimental data.

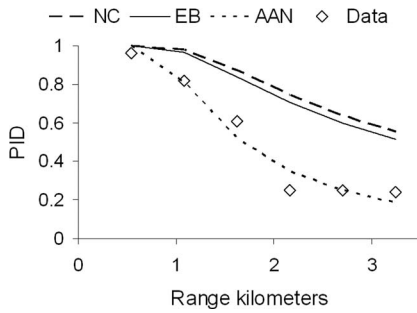


Fig. 10. PID versus range for experiment 25, line 1.

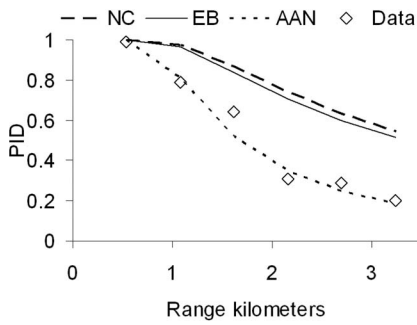


Fig. 11. PID versus range for experiment 25, line 2.

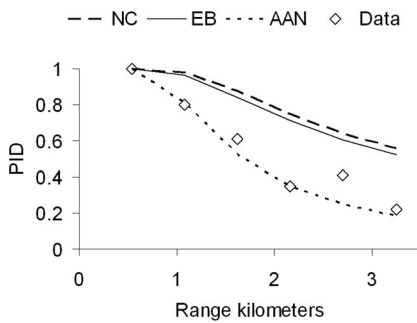


Fig. 12. PID versus range for experiment 25, line 3.

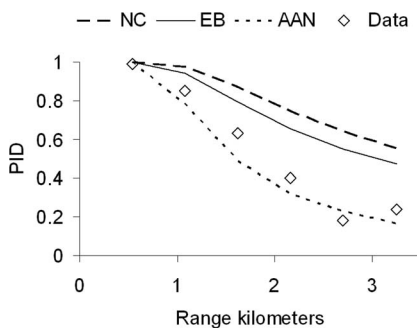


Fig. 13. PID versus range for experiment 25, line 4.

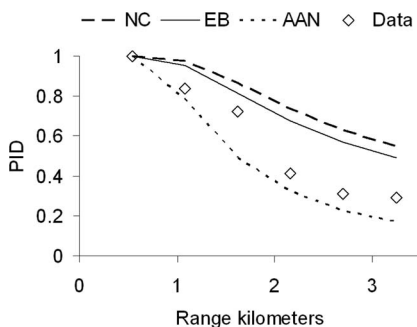


Fig. 14. PID versus range for experiment 25, line 5.

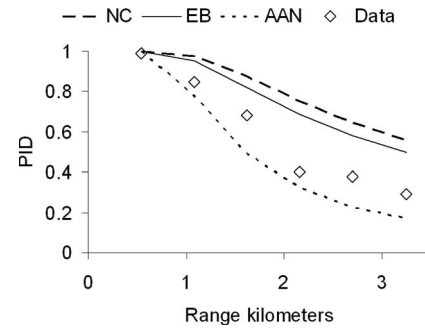


Fig. 15. PID versus range for experiment 25, line 6.

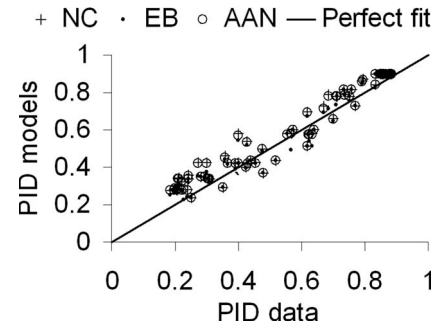


Fig. 16. Model predicted PID (ordinate) versus measured PID (abscissa) for experiment 21. The straight line represents a perfect fit between model and data. Display-to-eye distance is assumed to be fixed at 46 cm.

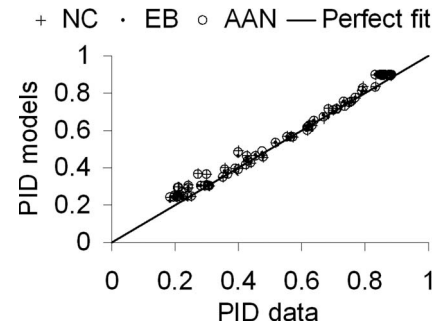


Fig. 17. Model predicted PID (ordinate) versus measured PID (abscissa) for experiment 21. Display-to-eye distance is allowed to vary between 30 and 75 cm.

6. CONCLUSIONS

This paper presents a new theory to predict the impact of sampling on target acquisition. Aliasing is treated as noise that has two unique characteristics. First, aliasing noise is proportional to target contrast. Second, the impact of aliasing on PID is range dependent. This is because sampling is constant in angle space, and targets become poorly sampled at long range.

Aliasing acts like noise because of the DRI task. At each range, observers attempt to identify a number of different targets. The effect of aliasing depends on sample phase, and the size and placement of identification cues varies from target to target. Aliasing acts like noise because of the combination of multiple target identifications, diversity in the size and placement of visual cues, and the random sample-phase of each target detail.

The AAN model uses the TTP metric to predict PID performance. The AAN model treats aliasing as noise that degrades the TTP value and therefore reduces PID. The

Table 3. Model Fit Criteria

| Experiment | NC to Model | | EB Model | | AAN Model | |
|------------|-------------|------|----------|------|-----------|------|
| | RMSE | COD | RMSE | COD | RMSE | COD |
| 21 | 0.036 | 0.91 | 0.026 | 0.94 | 0.034 | 0.92 |
| 25 | 0.272 | 0.08 | 0.231 | 0.33 | 0.089 | 0.90 |
| 36 | 0.216 | 0.46 | 0.174 | 0.65 | 0.081 | 0.92 |

same calibration factor α is used for both detector noise and aliasing noise. The combination of the experiments described here and the experiments described in [8] validate the TTP/AAN model for both well-sampled and poorly sampled imagery.

The AAN model accurately predicts the results of three sampling experiments. These experiments represent a variety of preblur, downsampling, postblur, and display configurations. The first experiment represents a typical low-resolution, midwave thermal imager. The experiment involves presenting the image using different display interpolations and system magnifications. The second experiment again uses a midwave thermal imager. In this experiment, however, imager performance with a large detector fill-factor is compared with performance when the detector fill-factor is unrealistically small. The small fill-factor resulted in an unrealistically large amount of aliasing. The third experiment involved applying various prefilters, downsampling, and postfilters to thermal images. The images were downsampled by as much as 25. In the third experiment, the angular size of the target at the eye remained constant regardless of downsample. That is, system magnification varied in order to keep displayed target size constant.

In all cases, AAN model predictions matched the experimental data quite well. COD was at least 0.90 for all experiments. Both near-range and far-range performance were accurately predicted. The AAN model correctly predicts the range curve for sampled imagers.

The model presented here does not predict the impact of sampling artifacts such as cathode ray tube (CRT) raster. An example of the artifact is shown in Fig. 18. Line raster hides the underlying image and degrades target acquisition performance. The CRT raster does not disappear



Fig. 18. Picture of clock showing how display raster can hide the underlying image.

as target contrast decreases to zero. The raster amplitude depends on average display luminance, not on target contrast.

It would be expected that the TTP metric predict the impact of display raster. To model CRT raster, the Fourier spectrum of the artifact is treated as fixed-pattern noise. However, the needed noise term is not currently calculated. This type of aliasing noise was not present in the sampling experiments.

We would expect that the AAN model predict the results of the character recognition experiment described in [1]. Each character is dithered to randomize sample-phase before sampling. Since the probability of character recognition is the fraction of characters recognized out of a large set, the impact of aliasing on recognition should be random. However, characters do not form a good DRI target set. Applying the AAN model to character recognition requires a different analysis from that presented in this paper.

APPENDIX A: GLOSSARY OF TERMS AND ACRONYMS

This glossary is in alphabetical order with Greek symbols at the end.

| | |
|--------------------|--|
| a | horizontal detector pitch |
| AAN | aliasing-as-noise model |
| A | Fourier transform of aliased signal |
| b | vertical detector pitch |
| B | noise filters in visual cortex |
| CTF | contrast threshold function |
| CTF_{sys} | CTF degraded by imager blur and noise |
| C_{TGT} | target signature expressed as contrast |
| DRI | detect, recognize, and identify model |
| D | postsample MTF |
| EB | equivalent blur model |
| FOV | field-of-view |
| FPA | focal plane array |
| H_{eye} | eyeball MTF |
| H_{pre} | presample MTF |
| H_{sys} | system MTF |
| ID | tactical-vehicle identification |
| I | Fourier transform of object radiance |
| L | luminance of the display in fL |
| MTDP | minimum temperature difference perceived |
| MTF | modulation transfer function |
| O | Fourier transform of sampled image |
| PID | probability of correct identification |
| Q | noise bandwidth |
| R_{ng} | range in kilometers |

| | |
|-----------------------|--|
| RSS | root sum squared |
| SCN | scene radiance that generates L |
| smag | system magnification |
| SOM | specific object model |
| SRR | spurious response ratio |
| SSD | signal spectral density |
| T_{con} | target radiance contrast |
| t_{eye} | eye integration time |
| TOD | triangle orientation discrimination |
| TTP | targeting task performance metric |
| w_a | square root of angle that object subtends at eye |
| α | a proportionality constant |
| γ | vertical sample frequency |
| δ | probability of seeing sine wave amplitude C_{TGT} |
| η | vertical spatial frequency |
| η_m | vertical spatial frequency |
| ν | horizontal sample frequency |
| ξ | horizontal spatial frequency |
| ξ_m | horizontal spatial frequency |
| Γ_{det} | noise standard deviation |
| Φ | value of TTP metric at range R_{ng} |
| Φ_{84} | value of TTP needed for 0.84 PID |

REFERENCES

1. R. G. Driggers, R. H. Vollmerhausen, and B. O'Kane, "Character recognition as a function of spurious response," *J. Opt. Soc. Am. A* **16**, 1026–1033 (1999).
2. R. Vollmerhausen, R. G. Driggers, and B. L. O'Kane, "Influence of sampling on target recognition and identification," *Opt. Eng. (Bellingham)* **38**, 763–772 (1999).
3. S. Park and R. Hazra, "Aliasing as noise: a quantitative and qualitative assessment," *Proc. SPIE* **1969**, 54–65 (1993).
4. R. H. Vollmerhausen and R. G. Driggers, *Analysis of Sampled Imaging Systems* (SPIE Press, 2000).
5. S. K. Moyer, R. G. Driggers, R. H. Vollmerhausen, and K. A. Krapels, "Target identification performance as a function of spurious response; aliasing with respect to the half sample rate," *Proc. SPIE* **4372**, 51–61 (2001).
6. W. Wittenstein, "Minimum temperature difference perceived—a new approach to assess undersampled thermal imagers," *Opt. Eng. (Bellingham)* **38**, 773–781 (1999).
7. P. Bijl and J. M. Valetton, "Triangle orientation discrimination: the alternative to minimum resolvable temperature difference and minimum resolvable contrast," *Opt. Eng. (Bellingham)* **37**, 1976–1983 (1998).
8. R. H. Vollmerhausen, E. Jacobs, and R. G. Driggers, "New metric for predicting target acquisition performance," *Opt. Eng. (Bellingham)* **43**, 2806–2818 (2004).
9. R. Vollmerhausen and A. L. Robinson, "Modeling target acquisition tasks associated with security and surveillance," *Appl. Opt.* **46**, 4209–4221 (2007).
10. R. H. Vollmerhausen, E. Jacobs, J. Hixson, and M. Friedman, "The targeting task performance (TTP) metric: a new model for predicting target acquisition performance," Tech. Rep. (DTIC AMSEL-NV-TR-230, U.S. Army Research, Development and Engineering Command, Communications and Electronics Research, Development and Engineering Center, Night Vision and Electronic Sensors Directorate, 10221 Burbeck Rd., Ft. Belvoir, VA 22060-5806, 2005).
11. P. G. J. Barten, "Formula for the contrast sensitivity of the human eye," *Proc. SPIE* **5294**, 231–238 (2004).
12. R. Vollmerhausen, "Incorporating display limitations into night vision performance models," in *IRIS Passive Sensors, Proceedings of the Infrared Information Symposium* (Environmental Research Institute of Michigan, 1995), Vol. 2, pp. 11–31.
13. R. Vollmerhausen, "Modeling the performance of imaging sensors," in *Electro-Optical Imaging: System Performance and Modeling*, Lucien M. Biberman, ed. (SPIE Press, 2000), pp. 12-1–12-41.
14. I. Overington, *Vision and Acquisition* (Crane, Russak & Co., 1976).
15. R. H. Vollmerhausen, S. Moyer, K. Krapels, R. G. Driggers, J. G. Hixson, and A. L. Robinson, "Predicting the probability of facial identification using a specific object model," *Appl. Opt.* **47**, 751–759 (2008).